2008 IEEE International Conference on
Robotics and Automation
Pasadena, CA, USA, May 19-23, 2008

Dynamic Stability of Off-Road Vehicles: Quasi-3D Analysis

Moshe Mann and Zvi Shiller

Abstract— **This paper presents a method to determine the stability of off-road vehicles moving on rough terrain. The measures of stability are defined as the maximum speed and acceleration under which the vehicle does not slide or tip over. To compute these stability measures, we propose a *quasi* 3D analysis by decomposing the vehicle dynamics into three separate planes: the yaw, pitch, and roll planes. In each plane, we compute the set of admissible speeds and acceleration for the planar vehicle model, contact model, and ground force constraints. The intersection of the admissible sets provides the total range of feasible speeds and accelerations along the vehicle's path, from which we obtain the stability margins. Numerical results for a vehicle traversing a simulated terrain demonstrate the effectiveness of the approach.**

I. Introduction

Many current missions require an autonomous robot to traverse rough terrain in minimum time, such as the DARPA's Grand Challenge [1]. The risk of instability becomes a crucial factor in its motion planning when both speed and terrain roughness are significantly high. The robot's susceptibility to slide, tip over, or lose contact with the ground increase with its speed and unevenness of the ground. Analyzing and ensuring the stability of the robot or vehicle at nonzero speeds is the goal of this work.

The success of a motion planner demonstrably depends on keeping the velocities and accelerations of the vehicle within their admissible range. Our goal is to compute the range of feasible speeds and accelerations for off road vehicles and present it as a unified measure of dynamic stability. Although various stability margins have been proposed over the years, [9] [3], none of them consider vehicle dynamics, friction constraints, and terrain surface characteristics, and hence are not suitable to evaluate vehicle stability during high speed motion on rough terrain. A few motion planners take into account only the geometry of the terrain [5], and of the vehicle [13][14] [4]. These planners, however, assume quasistatic motion, where the vehicle's speed is considered negligible.

The first dynamic motion planner for off road vehicles was developed in [10]. It calculates the global optimal trajectory for a point mass vehicle on general three dimensional terrain. This paper extends [10] and [8] to a 3D vehicle model. The approach consists of projecting the vehicle's motion onto three planes: the yaw, pitch, and roll planes, and then analyzing each plane separately. The velocity and acceleration limits are computed for each plane using a vector-algebraic procedure, and are then combined to yield the total dynamic stability margins.

The authors are with the Department of Mechanical Engineering and Mechatronics, The Paslin Robotics Research Laboratory, Ariel University Center, Ariel 40700, Israel. This work was partly supported by grant 01-99-08430 of the Israeli Space Agency through the Ministry of Science Culture and Sports of Israel. shiller@ariel.ac.il

II. Three dimensional terrain and vehicle model

A. Coordinate systems

Figure 1 shows the global and vehicle fixed coordinate frames. The vehicle travels along a path parameterized by its arc length s, such that its center of mass along the path is a parametric function of s. The vehicle's orientation along the path relative to the global frame is described by the rotation matrix R_B^0. The vehicle's angular velocity is expressed by rotations around the vehicle fixed frame, as shown in Figure 1.

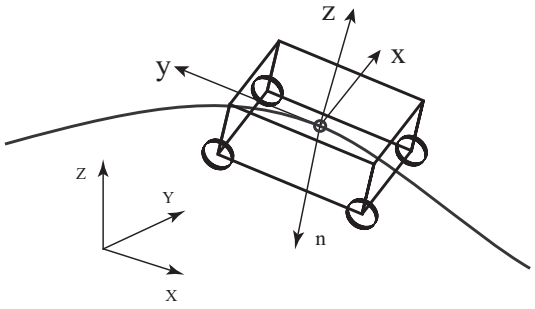

Fig. 1. World and body fixed coordinate frames

B. Angular velocities

The vehicle's angular velocity ω is computed by differentiating the rotation matrix of its body fixed frame relative to the inertial frame ([15]):

$$S(\omega) = {R_B^0}^T \dot{R}_B^0 \tag{1}$$

where $S(\omega)$ is a skew symmetric matrix, consisting of the elements of ω, and $\dot{R}_B^0$ is approximated by the finite differences of two successive rotation matrices along the path.

C. Path coordinates

To facilitate the analysis of the vehicle's stability, the acceleration of its center of mass, $\ddot{\mathbf{x}}$, is best described in terms of its speed $\dot{s}$ and acceleration $\ddot{s}$ along the path:

$$\ddot{\mathbf{x}} = \ddot{s}\mathbf{t} + (\dot{s}^2/\rho)\mathbf{n} \tag{2}$$

where $\mathbf{t}$ is a unit vector tangent to the path, $\mathbf{n}$ is a unit vector normal to the path and pointing towards the center of path curvature, as shown in Figure 1, and ρ is the radius

of curvature. The vehicle's angular speed and acceleration are expressed as:

$$\omega = \Theta_s \dot{s} \tag{3}$$

$$\dot{\omega} = \Theta_s \ddot{s} + \Theta_{ss} \dot{s}^2 \tag{4}$$

where Θ_s is obtained by differentiating R_B^0 with respect to s:

$$S(\Theta_s) = {R_B^0}^T (R_B^0)_s \tag{5}$$

and Θ_{ss} is its partial derivative with respect to the arc length s.

D. Inverse kinematics

Given the terrain map and vehicle's location and orientation in the the inertial coordinate system, we wish to calculate the vehicle's orientation and the direction of the ground normals. To this end, we model the vehicle as a tricycle by lumping the two front wheels into one center wheel, located at $\mathbf{x}_f$. We leave the radius of the wheels out of the inverse kinematics problem since the equations are highly nonlinear when the normals at the three contact points are not parallel to each other. Once the contact points are calculated, we add the average height of the wheels to the vehicle to obtain an approximation of its actual position. This is a reasonable approximation for relatively smooth terrain.

Thus, given x_c and y_c of the vehicle's center and its yaw angle ψ, we solve for seven unknowns $(x_f, y_f, x_l, y_l, x_r, y_r, z_c)$, using three equations for the location of the center of mass in world coordinates:

$$\begin{bmatrix} x_c \\ y_c \\ z_c \end{bmatrix} = \begin{bmatrix} x_f \\ y_f \\ z_f \end{bmatrix} + R_B^0 \begin{bmatrix} 0 \\ -d \\ h \end{bmatrix}, \tag{6}$$

three kinematic chains

$$\|\mathbf{x}_f - \mathbf{x}_l\| = \sqrt{4d^2 + l^2} \tag{7}$$

$$\|\mathbf{x}_f - \mathbf{x}_r\| = \sqrt{4d^2 + l^2} \tag{8}$$

$$\|\mathbf{x}_l - \mathbf{x}_r\| = 2l, \tag{9}$$

and the yaw angle relation [2]

$$\sin(\psi) R^0_{B(2,2)} + \cos(\psi) R^0_{B(3,1)} = 0, \tag{10}$$

where d, l, and h are the vehicle half length, width, and height, respectively, and $\mathbf{x}_f, \mathbf{x}_r, \mathbf{x}_l$ are the locations of the front, right, and left wheel axles, respectively.

The steering angle is approximated by projecting the vehicle at each point along the path onto the previous vehicle's $x-y$ plane, then using the approach presented in [12].

III. Planar Projections

For the quasi 3D approach, we split the vehicle's motion into three separate planes: the yaw (ψ), pitch (θ), and roll (ϕ) planes, as shown in Figure 2, where β is the steering angle. The unit tangent vector $\mathbf{t}$, curvature vector κ, and gravity vector $\mathbf{g}$, are projected onto all three planes using the respective projection matrices:

$$R_\psi = \begin{bmatrix} \mathbf{e}_x^T \\ \mathbf{e}_y^T \end{bmatrix}, \quad R_\theta = \begin{bmatrix} \mathbf{e}_y^T \\ \mathbf{e}_z^T \end{bmatrix}, \quad R_\phi = \begin{bmatrix} \mathbf{e}_z^T \\ \mathbf{e}_x^T \end{bmatrix} \tag{11}$$

where $\mathbf{e}_x, \mathbf{e}_y, \mathbf{e}_z$ are the unit vectors comprising the vehicle's body fixed frame. The projections of the tangent, curvature,

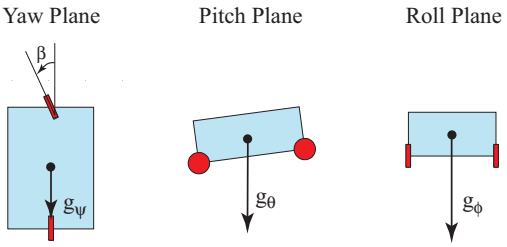

Fig. 2. Vehicle as seen in the yaw, pitch, and roll planes

and gravity vectors in each plane are computed by pre-multiplying each vector by the respective projection matrix.

IV. Contact Model

To maintain contact with the ground, without slip, the contact force between the wheel and the ground must be confined to the elliptic friction cone shown in Figure 3:

$$\frac{\mathbf{f}_s^2}{\mu_s^2} + \frac{\mathbf{f}_r^2}{\mu_r^2} \leq f_n^2 \tag{12}$$

where μ_s and μ_r are the longitudinal and lateral coefficients of friction, and $\mathbf{f}_n$ is the normal force applied by the ground.

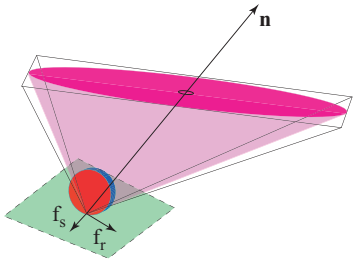

Fig. 3. The ground forces on the wheels are bounded by a conic ellipsoid.

The elliptic cone projects onto the yaw plane as an ellipsoid, and onto the pitch and roll planes as a friction cone. The cone is linearly approximated as a pyramid, where the friction constraints are reduced to:

$$f_s \leq \mu_s f_n \tag{13}$$

$$f_s \geq -\mu_s f_n \tag{14}$$

$$f_r \leq \mu_r f_n \tag{15}$$

$$f_r \geq -\mu_r f_n \tag{16}$$

This approximation, though not conservative, allows us to easily solve for the feasible speeds and accelerations.

V. Equations of Motion

Both the vehicle dimensions and the ground forces are projected onto the pitch, roll, and yaw planes, with the respective plane indicated by the subscript.

A. Pitch Plane

The forces acting on the lateral plane of the vehicle undergoing longitudinal motion are shown in Figure 4. The equations of motion are:

$$\mathbf{f}_{1\theta} + \mathbf{f}_{2\theta} + m\mathbf{g}_\theta = m\mathbf{t}_\theta \ddot{s} + m\kappa_\theta \dot{s}^2 \quad (17)$$

$$\mathbf{r}_{1\theta} \times \mathbf{f}_{1\theta} + \mathbf{r}_{2\theta} \times \mathbf{f}_{2\theta} = I_\theta(\theta_s \ddot{s} + \theta_{ss}\dot{s}^2) \quad (18)$$

where I_θ is the moment of inertia around the pitch plane.

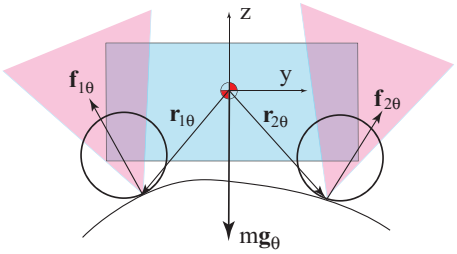

Fig. 4. The vehicle in the pitch plane.

The friction cones shown represent (15)-(16).

B. Roll Plane

Similarly, for the roll plane shown in Figure 5, we have:

$$\mathbf{f}_{1\phi} + \mathbf{f}_{2\phi} + m\mathbf{g}_\phi = m\mathbf{t}_\phi \ddot{s} + m\kappa_\phi \dot{s}^2 \quad (19)$$

$$\mathbf{r}_{1\phi} \times \mathbf{f}_{1\phi} + \mathbf{r}_{2\phi} \times \mathbf{f}_{2\phi} = I_\phi(\phi_s \ddot{s} + \phi_{ss}\dot{s}^2) \quad (20)$$

Note that $\mathbf{t}_\phi$ is rather small, since the path direction is generally almost perpendicular to the pitch plane. The friction cones shown represent constraints (13)-(14).

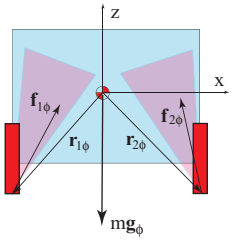

Fig. 5. The vehicle in the roll plane.

C. Yaw Plane

The vehicle is modeled in the yaw plane as a bicycle, as shown in Figure 6. We make a simplifying assumption that the normal force in the yaw plane on each wheel is half of the gravitational force mg_k normal to the plane, where:

$$g_k = -\mathbf{g} \cdot \mathbf{e}_z \quad (21)$$

Constraints (13)-(16) then become:

$$-\mu_r \frac{1}{2} m g_k \leq \quad f_r \quad \leq \mu_r \frac{1}{2} m g_k \quad (22)$$

$$-\mu_s \frac{1}{2} m g_k \leq \quad f_s \quad \leq \mu_s \frac{1}{2} m g_k \quad (23)$$

These constraints are linear approximations of the projected friction ellipses shown in Figure 6. The resulting equations

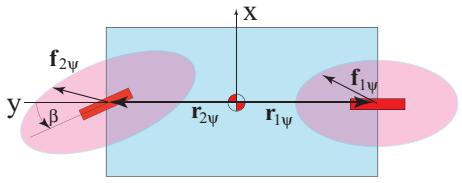

Fig. 6. The vehicle in the yaw plane.

of motion are:

$$\mathbf{f}_{1\psi} + R(\beta)\mathbf{f}_{2\psi} + m\mathbf{g}_\psi = m\mathbf{t}_\psi \ddot{s} + m\kappa_\psi \dot{s}^2 \quad (24)$$

$$\mathbf{r}_{1\psi} \times \mathbf{f}_{1\psi} + \mathbf{r}_{2\psi} \times (R(\beta)\mathbf{f}_{2\psi}) = I_\psi(\psi_s \ddot{s} + \psi_{ss}\dot{s}^2) \quad (25)$$

where

$$R(\beta) = \begin{bmatrix} \cos(\beta) & -\sin(\beta) \\ \sin(\beta) & \cos(\beta) \end{bmatrix} \quad (26)$$

VI. Solution Method

To determine the constraints on the vehicle's speed and acceleration, we map the contact force constraints onto constraints on $\ddot{s}$ and $\dot{s}$. Because this problem is indeterminate, since in each plane we have three equations of motion and four unknowns, we substitute the proper combination of ground force constraints into the equations of motion to result in linear constraints in the $\ddot{s} - \dot{s}^2$ plane. The solution method in the pitch and roll plane is equivalent to [7], and we review it here to extend it in a similar manner to the yaw plane. The graphical approach [6] is another convenient way to solve the problem.

A. Pitch

A planar friction cone C may be expressed as an intersection of two half planes. Any ground force $\mathbf{f}_\theta \in C$ can be expressed as a linear combination of the unit vectors $\mathbf{e}$ parallel and $\mathbf{n}$ normal to the boundary of the left and right half planes, as illustrated in Figure 7:

$$\mathbf{f}_\theta = k_l \mathbf{e}_l + c_l \mathbf{n}_l \quad (27)$$

$$\mathbf{f}_\theta = k_r \mathbf{e}_r + c_r \mathbf{n}_r \quad (28)$$

For $\mathbf{f}_\theta$ to be in C, the coefficients in (27, 28) must simultaneously satisfy the two inequality constraints:

$$c_l \geq 0 \quad (29)$$

$$c_r \geq 0. \quad (30)$$

Since (29, 30) apply to each contact point, there are a total of four such constraints for the (planar) vehicle.

We now substitute the ground forces, each represented by one half plane of its friction cone, (27) or (28), into the equations of motion (17)-(18) to result in three equations in four unknowns (k_1, c_1, k_2, c_2). Eliminating two unknowns (k_1, k_2) produces one equation in two unknowns (c_1, c_2) of the form:

$$a_1 \ddot{s} + a_2 \dot{s}^2 + (a_3 c_1 + a_4 c_2 + a_5) = 0 \quad (31)$$

where:

$$\begin{aligned} [a_1 \quad a_2] \quad &= \quad m[\mathbf{r}_{1\theta} \times \mathbf{e}_1 \quad \mathbf{r}_{2\theta} \times \mathbf{e}_2] \\ &- \quad I_\theta[\theta_s \quad \theta_{ss}][\mathbf{e}_1 \quad \mathbf{e}_2]^{-1}[\mathbf{t}_\theta \quad \kappa_\theta] \end{aligned} \quad (32)$$

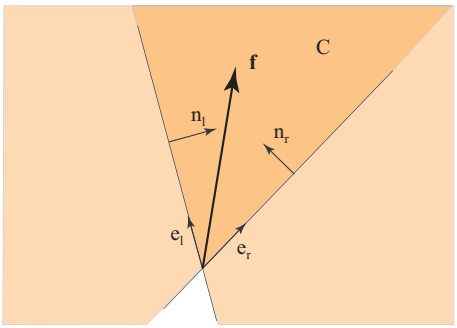

Fig. 7. Each friction cones is the intersection of two half planes.

$$[a_3 \quad a_4] = [\mathbf{r}_{1\theta} \times \mathbf{n}_1 \quad \mathbf{r}_{2\theta} \times \mathbf{n}_2] - [\mathbf{r}_{1\theta} \times \mathbf{e}_1 \quad \mathbf{r}_{2\theta} \times \mathbf{e}_2][\mathbf{e}_1 \quad \mathbf{e}_2]^{-1}[\mathbf{n}_1 \quad \mathbf{n}_2] \tag{33}$$

$$a_5 = -[\mathbf{r}_{1\theta} \times \mathbf{e}_1 \quad \mathbf{r}_{2\theta} \times \mathbf{e}_2][\mathbf{e}_1 \mathbf{e}_2]^{-1} m\mathbf{g}. \tag{34}$$

Equation (31) represents a straight line in the $\ddot{s} - \dot{s}^2$ plane for given c_1, c_2. If $a_3 a_4 > 0$, then varying c_1, c_2 from 0 to ∞ would span a half plane in the $\ddot{s} - \dot{s}^2$ space. Thus, (31) maps the selected force constraints (the two half planes) on $\mathbf{f}_{1\theta}$ and $\mathbf{f}_{2\theta}$ to constraints on $\ddot{s} - \dot{s}^2$. Repeating (31) for all possible combinations of half planes of the rear and front friction cones would produce four half planes in the $\ddot{s} - \dot{s}^2$ space. The intersection of these half planes represents the set of admissible speeds and accelerations that satisfy all the ground force constraints. This will be further discussed in Section VII.

B. Roll

The set of admissible speeds and accelerations due to constraints on the ground forces in the roll plane are obtained similarly to the procedure outlined for the pitch plane, except that we now use the friction cones and equations of motion of the roll plane (17- 18).

C. Yaw

In a similar manner, the rectangular approximation of the friction ellipsoid in the yaw plane can be visualized as the intersection of four half planes, whose edges form the right, top, left, and bottom edges of the friction rectangle R, as shown in Figure 8, where $\mathbf{e}_r$ and $\mathbf{e}_s$ are the unit vectors in the respective rolling and lateral directions, and $\mathbf{n}_r$ and $\mathbf{n}_s$ (not shown) are the respective normals. Any force $\mathbf{f}_\psi \in R$ must belong to the following four half planes:

$$\mathbf{f}_\psi = k_r \mathbf{e}_r + (\frac{1}{2}\mu_s m g_k - c_r)\mathbf{n}_r \tag{35}$$

$$\mathbf{f}_\psi = k_t \mathbf{e}_s + (\frac{1}{2}\mu_r m g_k - c_t)\mathbf{n}_s \tag{36}$$

$$\mathbf{f}_\psi = k_l \mathbf{e}_r + (-\frac{1}{2}\mu_s m g_k + c_l)\mathbf{n}_r \tag{37}$$

$$\mathbf{f}_\psi = k_b \mathbf{e}_s + (-\frac{1}{2}\mu_r m g_k + c_b)\mathbf{n}_s \tag{38}$$

For $\mathbf{f}_\psi$ to be in R, it is necessary that the coefficients in (35-38) simultaneously satisfy the inequality constraints:

$$c_r \geq 0 \tag{39}$$

$$c_t \geq 0 \tag{40}$$

$$c_l \geq 0 \tag{41}$$

$$c_b \geq 0 \tag{42}$$

Substituting one of equations (35-38) for each wheel into the equations of motion (24,25) and eliminating two unknowns yields a scalar equation in $\ddot{s}, \dot{s}^2$ similar to (31), with the coefficients:

$$[a_1 \quad a_2] = [\mathbf{r}_1 \times \mathbf{e}_1 \quad \mathbf{r}_2 \times \mathbf{e}_2][\mathbf{e}_1 \quad \mathbf{e}_2]^{-1} - I_\psi[\psi_s \quad \psi_{ss}] \tag{43}$$

$$[a_3 \quad a_4] = [\mathbf{r}_1 \times \mathbf{n}_1 \quad \mathbf{r}_2 \times \mathbf{n}_2] - [\mathbf{r}_{1\psi} \times \mathbf{e}_1 \quad \mathbf{r}_{2\psi} \times \mathbf{e}_2][\mathbf{e}_1 \quad \mathbf{e}_2]^{-1}[\mathbf{n}_1 \quad \mathbf{n}_2] \tag{44}$$

$$a_5 = ([\mathbf{r}_{1\psi} \times \mathbf{n}_1 \quad \mathbf{r}_{2\psi} \times \mathbf{n}_2] - [\mathbf{r}_{1\psi} \times \mathbf{e}_1 \quad \mathbf{r}_{2\psi} \times \mathbf{e}_2][\mathbf{e}_1 \quad \mathbf{e}_2]^{-1}) \begin{bmatrix} \mu_1 \\ \mu_2 \end{bmatrix} - [\mathbf{r}_{1\psi} \times \mathbf{e}_1 \quad \mathbf{r}_{2\psi} \times \mathbf{e}_2][\mathbf{e}_1 \quad \mathbf{e}_2]^{-1} m\mathbf{g}_\psi \tag{45}$$

where $\mathbf{e}_1, \mathbf{e}_2, \mathbf{n}_1, \mathbf{n}_2, \mu_1, \mu_2$ are selected for every combination

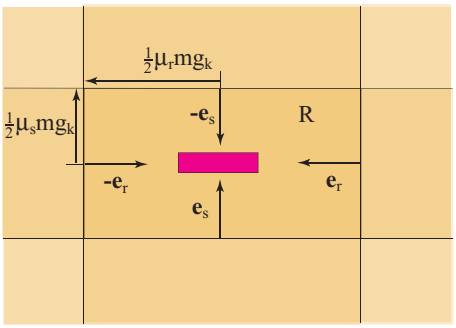

Fig. 8. The friction rectangle in the yaw plane is the intersection of four half planes.

of half planes that contain the ground forces on each wheel.

VII. Stability Margins

Intersecting the half planes in the $\ddot{s} - \dot{s}^2$ space, produced by all combinations of the ground force constraints in each of the three planes, results in the set of Feasible Speeds and Acceleration (FSA), shown schematically in Figure 9 [11]. Any given pair of speed and acceleration that lies outside of the FSA region is unattainable, i.e. violates at least one contact constraint. We define the dynamic stability margin (DSM) as the maximum feasible speed, and the static stability margin (SSM), as the minimum feasible acceleration range at zero speed along every point of the path, s, as shown in Figure 9, where the stability margins are indicated by the boundaries of the FSA:

$$DSM(s) = \begin{cases} max(\dot{s}), \dot{s}^2 \in FSA & \text{if } max(\dot{s}) \geq 0 \\ 0 & \text{otherwise} \end{cases} \tag{46}$$

$$SSM(s) = \begin{cases} min(|\ddot{s}_{min}|, |\ddot{s}_{max}|)_{\dot{s}=0} & \text{if } \ddot{s}_{max} > 0,\ \ddot{s}_{min} < 0 \\ = 0 & \text{otherwise} \end{cases} \quad (47)$$

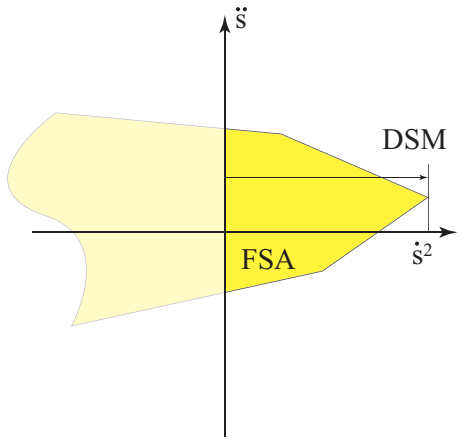

Fig. 9. The Feasible range of Speed and Acceleration (FSA) with the Static Stability Margin(SSM) and the Dynamic Stability Margin (DSM).

The SSM and DSM are important indicators of the stability of a vehicle traversing a preset trajectory. For example, a vehicle on a steep incline will have a low SSM, indicating that slippage is likely to occur if the vehicle accelerates too rapidly. A vehicle on a convex surface will have a low DSM, which indicates that a sufficiently high velocity will result in the vehicle losing contact with the surface.

VIII. Examples

To demonstrate the utility of the FSA and stability margins, we simulate a three dimensional vehicle model traversing a serpentine path on a random crater and hill, as shown in Figure 10. The vehicle is illustrated as a tricycle in concurrence with its kinematic model. The three separate

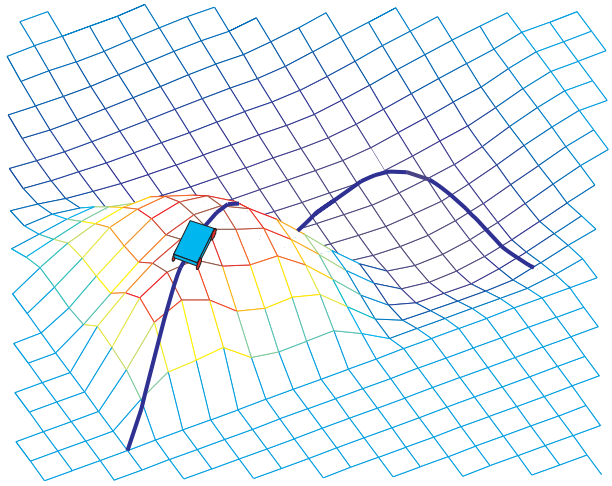

Fig. 10. A vehicle traversing a crater and a hill

FSA's for each pitch, roll, and yaw plane, are shown in Figure 11 for the point at which the vehicle is at the top of the hill in Figure 10. One sees from Figure 11 that at this point the static stability margin in the yaw plane is the most restrictive, as its FSA is a narrow polygon. The roll plane, on the other hand, is the least restrictive. The orientations of the

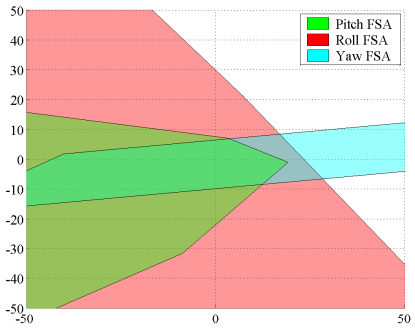

Fig. 11. The FSA's for each plane

vehicle in each plane are shown in Figure 12. Matching the configuration in the pitch plane with the corresponding FSA indicates that the result is in good agreement with previous two dimensional stability analysis [8], as a vehicle on convex ground is expected to have a finite velocity limit. The SSM

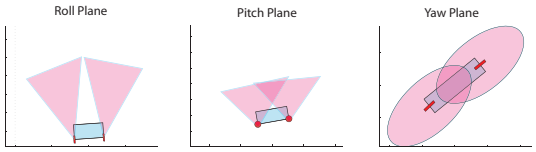

Fig. 12. The vehicle's orientation in the pitch, yaw, and roll planes

and DSM for the entire trajectory are shown in Figure 13. As expected, the yaw motion is the most constraining along most of the path, and the yaw stability margins are at their lowest when the vehicle makes a turn in the crater. For the case shown, the SSM drops to zero along the downward slope towards the end of the path, indicating a slope too steep to sustain the vehicle in a static state. The pitch DSM is lowest at the top of the hill, and the roll SSM is monotonously high along the entire path.

Figure 14 shows the vehicle over a road bump. The DSM for this path is shown in Figure 15. The DSM drops as each wheel passes over the bump. It reaches around 1 m/s as the front wheel moves over the bump. Moving at any higher speeds would cause the font wheel to loose contact with the ground. The numerically computed velocity limit (DSM) was verified with a dynamic simulation of a vehicle with the same mass properties, moving over the speed bump at various speeds. Starting at $1m/s$, the vehicle moved over the bump without loosing contact with the ground, as expected. The degree of contact was determined by the minimum normal force developed between the front wheel and ground. Increasing the speed resulted in a lower normal force, until reaching zero, or separation between the front wheel and ground. Figure 16 shows the minimum normal force, normalized by the steady state normal force (roughly half the vehicle weight), as a function of the vehicle speed.

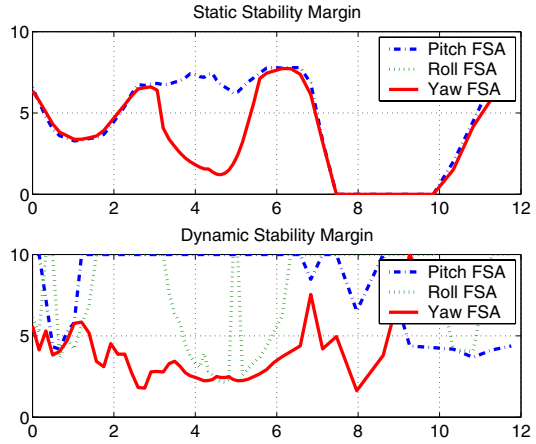

Fig. 13. The respective SSM's and DSM's for each vehicle model

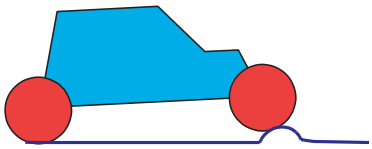

Fig. 14. A vehicle traversing a road bump

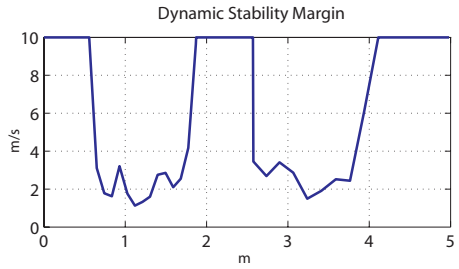

Fig. 15. The DSM for the road bump

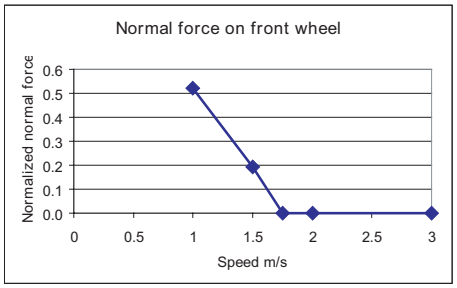

Fig. 16. Normal force on front wheel as a function of speed

The normal force drops to zero at $1.75m/s$. This is slightly higher than the $1m/s$ velocity limit predicted by our stability analysis. This difference is expected since the vehicle used in the dynamic simulation uses had suspension and inflated tires, whereas our vehicle model has no suspension and assumes rigid wheels.

Repeating the simulation for a smoother bump (not shown), resulted in a closer agreement between the simulated velocity at which separation begins and the computed velocity limit. Although these results are preliminary, they do validate the effectiveness of our approach to predicting the dynamic stability of road and off-road vehicles. Further studies are required to better understand the effect of suspension on the velocity limit.

IX. Conclusions

This paper presented a unified method for computing the range of feasible speeds and accelerations for an all terrain vehicle undergoing motion in three dimensions using the quasi-3D approach. The vehicle's motion is projected onto the yaw, pitch, and roll planes. The stability of the vehicle is analyzed in each separate plane by substituting the ground force constraints into the equations of motion for each plane. This produces the set of admissible speeds and acceleration (FSA) in each plane, which when overlayed results in the overall FSA. This in turn provides the static and dynamic stability margins along the path. An example of a vehicle moving along a curved path over mountainous terrain demonstrates the approach.

References

[1] Darpa's grand challenge. http://www.darpa.mil/grandchallenge/index.asp. as of March 2007.

[2] J. Craig. Appendix b. In *Introduction to Robotics: Mechanics and Control*. Prentice Hall, 2nd edition, 1989.

[3] E. Garcia, J. Estremera, and P.G. de Santos. Stability margins for walking machines. *Robotica*, 30:595–606, 2002.

[4] H. Hacot. The kinematic analysis and motion control of a planetary rover. Master's thesis, MIT, May 1998.

[5] A. Liegeois and Ch. Moignard. *Geometric reasoning for perception and action*. Springer Verlag, 1993.

[6] M. Mann and Z. Shiller. Dynamic stability of off road vehicles: A geometric approach. In *Proceedings of the IEEE International Conference on Robotics and Automation*, pages 3705–3710, May 2006.

[7] M. Mann and Z. Shiller. On the dynamic stability of off road vehicles. In *ROMANSY*, pages 3705–3710, May 2006.

[8] M.P. Mann. Dynamic stability of off road vehicles. Master's thesis, Technion, Israel Institute of Technology, Haifa, Israel, August 2007.

[9] R.B. McGhee and A.A. Frank. On the stability properties of quadruped creeping gaits. *Journal of Mathematical Biosciences*, 3(2):331–351, 1968.

[10] Z. Shiller and Y.R. Gwo. Dynamic motion planning of autonomous vehicles. In *IEEE Transactions on Robotics and Automation*, volume 7, pages 241–249, April 1991.

[11] Z. Shiller and M. Mann. Dynamic stability of off road vehicles. In *Proceedings of the IEEE/RSJ International Workshop on Intelligent Robots and Systems (IROS)*, pages 1849–1853, October 2004.

[12] Z. Shiller and S. Sundar. Emergency maneuvers of ahs vehicles. *Paper 951893, SAE Transactions, Journal of Passenger Cars*, 104:2633–2643, 1995.

[13] T. Simeon. Motion planning for a non-holonomic mobile robot on 3-dimensional terrain. In *Proceedings of the IEEE/RSJ International Workshop on Intelligent Robots and Systems*, pages 1455–1460, November 1991.

[14] T. Simeon and B. Dacre-Wright. A practical motion planner for all terrain mobile robot. In *Proceedings of the IEEE/RSJ International Workshop on Intelligent Robots and Systems*, July 1993.

[15] M.W. Spong, S. Hutchinson, and M. Vidyasagar. *Robot Modeling and Control*, chapter 2. John Wiley and Sons, 2005.